

Squeezed-Light-Enhanced Multiparameter Quantum Estimation in Cavity Magnonics

Hamza Harraf,¹ Mohamed Amazioug,^{2,*} and Rachid Ahl Laamara^{1,3}

¹*LPHE-Modeling and Simulation, Faculty of Sciences, Mohammed V University in Rabat, Rabat, Morocco*

²*LPTHE-Department of Physics, Faculty of sciences, Ibnou Zohr University, Agadir, Morocco*

³*Centre of Physics and Mathematics, CPM, Faculty of Sciences, Mohammed V University in Rabat, Rabat, Morocco*

(Dated: January 21, 2026)

Improving multiparameter quantum estimation in magnonic systems via quantum noise suppression is a well-established and critical research objective. In this work, we propose an experimentally realistic scheme to improve the precision of simultaneously estimating different parameters in a cavity-magnon system by utilizing a degenerate optical parametric amplifier (OPA). The OPA enhances the estimation precision by decreasing the most informative quantum Cramér-Rao bound, calculated employing the symmetric logarithmic derivative (SLD) and the right logarithmic derivative (RLD). We show that when nonlinearity is introduced into the system, quantum noise is significantly suppressed. Our results show how different physical parameters influence multiparameter estimation precision and provide a detailed discussion of the associated physical mechanisms in the steady state. Our results focus on exploring practical Gaussian measurement schemes that can be realized experimentally. Besides, we further analyze the system's dynamics, comparing both the SLD quantum Fisher information (QFI) and the classical Fisher information (CFI) for both homodyne and heterodyne detection. This approach provides a robust foundation for multiparameter quantum estimation, offering significant potential for application in hybrid magnomechanical and optomechanical systems.

I. INTRODUCTION

Gaussian states within continuous-variable (CV) frameworks [1–3] have become prominent in quantum information for two main reasons: their theoretical description is simplified by the use of only first and second moments, and they are readily generated and controlled in experimental setups. These states can be implemented in various protocols, ranging from quantum optomechanics [4–9] and teleportation channels [10] to recent advances in magnomechanics [11, 12]. Additionally, the Gaussian framework is justified by its successful application in key experimental milestones, such as studies on Bose-Einstein condensates [13–15] and the high-precision detection of gravitational waves [16].

Within the rapidly developing field of condensed matter physics, cavity magnonics has emerged to study the coherent coupling between photons and quantized collective spin excitations, known as magnons [17–23]. Due to their quantized nature in magnetically ordered systems, magnons offer efficient interaction with external magnetic fields and provide the advantage of highly tunable operational frequencies. Furthermore, magnons offer a powerful framework for implementing hybrid quantum systems with enhanced controllability, owing to their coherent coupling across a wide range of platforms. Their ability to serve as high-fidelity carriers for quantum information processing has further established their prominence in the field [24]. The adoption of yttrium iron garnet (YIG) spheres has facilitated the study of magnonic interactions within a high-precision regime. The combination of dense spin populations and low damping [25–32] positions these spheres as excellent candidates for implementing quantum information and metrological protocols [25, 33]. Experimental progress has established magnon-based sensing as a high-precision tool, utilizing dispersive coupling with superconducting qubits [34]. Additionally, experiments in cavity magnonic systems have validated the magnetic dipole-mediated coupling between magnons and microwave cavity modes [25–27, 35, 36]. Notably, such interactions are not limited by thermal constraints, as they can be experimentally realized in YIG systems operating at both cryogenic [25, 27, 35, 36] and room temperatures [26, 35]. Additionally, the versatility of this coupling is demonstrated by the observation of the Purcell effect and magnetically induced transparency [26]. Such interactions are particularly crucial in cavity magnomechanical systems [37, 38]; here, magnons couple to microwave photons through magnetic dipoles while simultaneously interacting with phonons via magnetostriction. Furthermore, various quantum protocols have been implemented within this framework, including microwave-to-optical transduction [39], the engineering of quantum entanglement [40–50], magnon blockade [51, 52] and the generation of squeezed magnonic and photonic states [53, 54]. Additional applications encompass phononic lasing [55], quantum sensing specifically thermometry [56] and magnetometry [57–59] as well as magnon blockade [60, 61], quantum illumination [62], and state-transfer processes such as photon–phonon conversion and quantum memory [63–65].

* m.amazioug@uiz.ac.ma

The Quantum Fisher Information Matrix (QFIM) originated from the work of Helstrom and Holevo [66–69] and was later refined and popularized by Braunstein and Caves [70]. The QFIM aims to describe the limits of distinguishability for quantum states characterized by infinitesimally different parameters. Within the field of multiparameter quantum metrology, this matrix represents a vital component, given that its inverse sets the boundary for the maximum precision attainable in joint parameter estimation. Investigating the enhancement of the QFIM is thus crucial for the advancement of multiparameter quantum metrology. However, the ultimate precision dictated by the quantum Cramér-Rao bound (QCRB) [71] is not universally saturable, often hindered by experimental realities or inherent mathematical constraints in the multiparameter regime [72]. Despite these limitations, the QCRB provides a benchmark to evaluate whether a proposed quantum detector is viable and if it can surpass the precision limits of current technological standards [73–76]. Unlike multiparameter scenarios, the QCRB is always achievable for single-parameter estimation. This theoretical certainty underpins numerous advancements, ranging from gravitational wave sensing [77] and quantum thermometry [78, 80] to the precise measurement of phase, squeezing parameters, time, and frequency [81–84]. Conversely, the simultaneous estimation of multiple parameters often fails to saturate the QCRB. This is primarily due to the non-commutativity of the optimal observables, which creates an incompatibility between the measurement schemes required to achieve maximum precision for different parameters [85–89]. To address these challenges, substantial effort has been devoted to multiparameter quantum metrology. The goal is to generalize the criteria under which the QCRB can be saturated, thereby enabling the simultaneous estimation of multiple variables with maximum achievable accuracy. The QFIM is also closely connected to the quantification of key quantum properties, such as coherence and entanglement [84, 90–94]. These potential applications underscore the importance of developing precise theoretical techniques for computing the QFIM. This work addresses that need by introducing an analytical method to obtain the QFIM for systems described by Gaussian-type bosonic continuous variables.

In this work, we theoretically investigate the enhancement of the so-called the most informative quantum Cramér-Rao bound (BMI) within a feasible experimental scheme utilizing an optical parametric amplifier (OPA). The system under study consists of a cavity-magnonic system where magnons, acting as quantum excitations of spin waves, are coupled to microwave cavity photons via magnetic dipole interactions. Driven by an external classical field, the microwave cavity mode is analyzed using a set of feasible experimental parameters. Furthermore, we ensure that all reported results fall within the stable regime of the system's dynamics. Specifically, we show that the introduction of an OPA leads to an enhanced estimation regime where the BMI is minimized, allowing for higher precision. In the steady state, we explore the dependence of the estimated precisions of g_{mc} and γ_c on the system temperature, the magnon-photon coupling strength, the driving power, and the cavity and magnon detuning. In addition, we analyze the dynamics of the symmetric logarithmic derivative (SLD)-based QFIM and compare it with the Classical Fisher Information (CFI) obtained via homodyne and heterodyne detection. By evaluating these quantities, we establish the ultimate precision bounds for g_{mc} estimation and pinpoint the most effective measurement protocols. Consequently, we focus on exploring practical Gaussian measurement schemes that can be realized experimentally. Both homodyne and heterodyne detection [95, 96] represent fundamental Gaussian measurement strategies with significant applications in continuous-variable signal processing. Gaussian measurements on Gaussian states produce Gaussian-distributed results, allowing the parameters of interest to be determined from the statistical moments of the quadrature operators. Moreover, we investigate the comparative performance of homodyne and heterodyne detection for the estimation of g_{mc} and γ_c , using the ultimate precision limit of optimal measurement settings as a performance benchmark.

This article is organized as follows. In Sec. II, we investigate the system dynamics using the quantum Langevin equations (QLEs). Section III focuses on the linearization of these equations and the derivation of the covariance matrix (CM) for both steady-state and dynamical regimes. Section IV gives the theoretical framework for multiparameter quantum estimation of Gaussian states; here, we derive the QFIM via the SLD and RLD operators, compare individual and simultaneous estimation strategies, and evaluate the classical Fisher information for homodyne and heterodyne detection. The numerical results are discussed in Sec. V. Finally, Sec. VI provides a summary of our findings along with concluding remarks and a future outlook.

II. THE MODEL

Fig. 1(a) depicts the proposed system, which consists of a second-order nonlinear $\chi^{(2)}$ cavity (e.g., lithium niobate or aluminum nitride [97–99]) and a YIG sphere. A static magnetic field H_z is applied to the YIG sphere to induce magnon excitations, which couple to the microwave cavity mode at a rate g_{mc} [25, 26, 100, 101]. In addition, the system incorporates a degenerate optical parametric amplifier (OPA) that pumps the cavity mode with a two-photon drive. Following the scheme shown in Fig. 1(c), the driving frequency is set to $\omega_d = 2\omega_c$, where ω_c represents the cavity's resonance frequency and θ denotes the pump phase. By considering an external electromagnetic drive applied to the cavity mode, we can write the system Hamiltonian as follows

$$H = \hbar\omega_c \hat{c}^\dagger \hat{c} + \hbar\omega_m \hat{m}^\dagger \hat{m} + \hbar g_{mc}(\hat{c} + \hat{c}^\dagger)(\hat{m} + \hat{m}^\dagger) + i\hbar\epsilon_L(\hat{c}^\dagger e^{-i\omega_0 t} - \hat{c} e^{i\omega_0 t}) + i\lambda\hbar(e^{-i\omega_d t} e^{i\theta} \hat{c}^{\dagger 2} - e^{i\omega_d t} e^{-i\theta} \hat{c}^2). \quad (1)$$

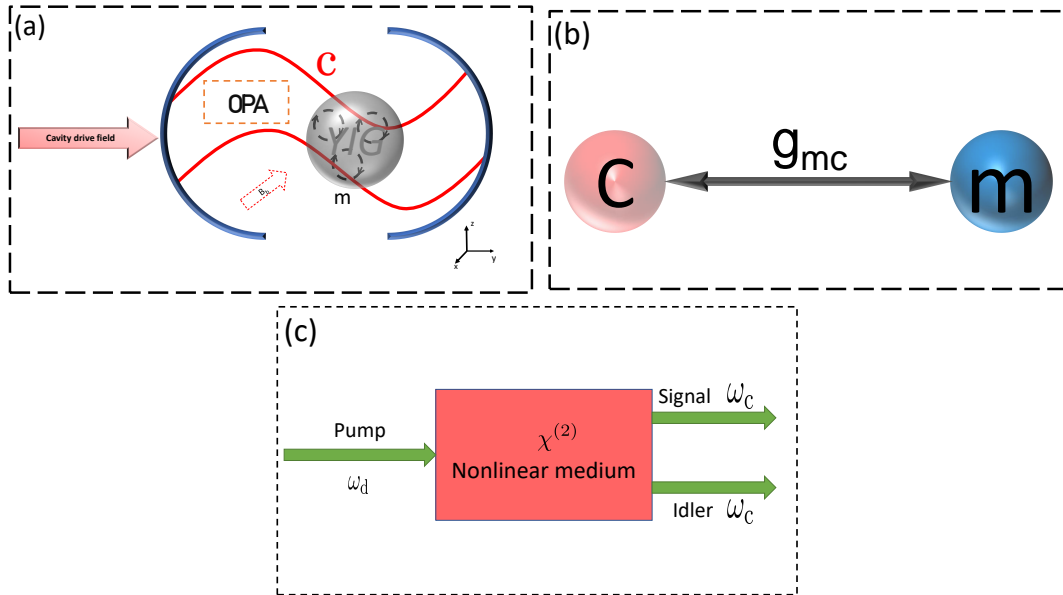


FIG. 1. (a) Schematic representation of the cavity-magnon system, with a YIG sphere positioned at the magnetic field antinode of the microwave cavity mode to maximize coupling. A uniform magnetic field \mathbf{B} is applied to bias the YIG sphere, with its orientation including at least one component parallel to the z -axis. Moreover, an external electromagnetic field drives the cavity mode. (b) The interaction between the photon mode and the magnon mode presents by cavity-magnon coupling g_{mc} . (c) The system utilizes a degenerate optical parametric amplifier (OPA) process where, mediated by second-order nonlinearity, a single pump photon of frequency ω_d is converted into two cavity photons of frequency ω_c (signal and Idler with same frequency ω_c). This process is governed by the resonance relation $\omega_d = 2\omega_c$.

The free-energy contribution of the system is captured by the first two terms of the Hamiltonian. The photonic and magnonic modes are described by the bosonic operators \hat{c} and \hat{m} , which satisfy the fundamental commutation relation $[\hat{o}, \hat{o}^\dagger] = 1$ (where $\hat{o} \in \{c, m\}$), with \hat{c}^\dagger and \hat{m}^\dagger being the corresponding creation operators. Moreover, ω_c (ω_m) represents the resonance frequency of the cavity (magnon) mode. Specifically, the magnonic resonance frequency $\omega_m = \gamma\mathbf{B}$ is governed by the external magnetic field \mathbf{B} . Given the gyromagnetic ratio $\gamma/2\pi = 28$ GHz/T, the magnon frequency can be readily tuned by adjusting the strength of the bias field. Moreover, the Kerr nonlinear effect in the magnons arising from magnetocrystalline anisotropy is considered sufficiently small to be ignored. When the magnon-photon coupling strength g_{mc} dominates the respective decay rates γ_c and γ_m , the system reaches the strong-coupling regime ($g_{mc} > \gamma_c, \gamma_m$). This condition has been extensively explored in recent literature [102–105]. The third term of the Hamiltonian describes the microwave photon-magnon coupling originating from the magnetic dipole interaction. In the rotating wave approximation (RWA), the interaction Hamiltonian $g_{mc}(\hat{c} + \hat{c}^\dagger)(\hat{m} + \hat{m}^\dagger)$ simplifies to the beamsplitter-like form $g_{mc}(\hat{c}\hat{m}^\dagger + \hat{c}^\dagger\hat{m})$. This approximation remains valid in the regime where the resonance frequencies significantly exceed the coupling and decay rates ($\omega_c, \omega_m \gg g_{mc}, \gamma_c, \gamma_m$), a condition readily satisfied in current experimental setups [12].

The external drive contribution is captured by the fourth Hamiltonian term, where the cavity is driven by a microwave field of frequency ω_L and power \mathcal{P}_{in} . The resulting driving rate is defined as $\epsilon_L = \sqrt{2\mathcal{P}_{in}\gamma_c/\hbar\omega_L}$, with γ_c representing the cavity decay rate. In the last Hamiltonian term, the OPA process is parameterized by the gain λ and its drive phase θ . By adopting a frame rotating at the drive frequency ω_L through the unitary transformation $U(t) = \exp[-i\omega_L(\hat{c}^\dagger\hat{c} + \hat{m}^\dagger\hat{m})t]$, the total Hamiltonian is expressed as

$$\begin{aligned} \hat{H} &= U(t)H U^\dagger(t) - i\hbar U(t) \frac{\partial U^\dagger(t)}{\partial t} \\ &= \hbar\Delta_c \hat{c}^\dagger \hat{c} + \hbar\Delta_m \hat{m}^\dagger \hat{m} + \hbar g_{mc}(\hat{c}\hat{m}^\dagger + \hat{c}^\dagger\hat{m}) \\ &\quad + i\hbar\epsilon_L(\hat{c}^\dagger - \hat{c}) + i\lambda\hbar(e^{i\theta}\hat{c}^\dagger 2 - e^{-i\theta}\hat{c}^2), \end{aligned} \quad (2)$$

with the cavity and magnonic detunings defined as $\Delta_c = \omega_c - \omega_L$ and $\Delta_m = \omega_m - \omega_L$, respectively.

III. COVARIANCE MATRIX

The system dynamics, accounting for both dissipation and quantum fluctuations, are governed by the quantum Langevin equations (QLEs) for the cavity (\hat{c}) and magnon (\hat{m}) operators. The quantum Langevin equations for the magnon and cavity modes, including their damping rates ($\gamma_{m,c}$) and associated noise operators (\hat{m}^{in} , \hat{c}^{in}), are obtained from the Hamiltonian [Eq. (2)] as

$$\frac{d\hat{c}}{dt} = -(i\Delta_c + \gamma_c)\hat{c} - ig_{mc}\hat{m} + 2\lambda e^{i\theta}\hat{c}^\dagger + \epsilon_L + \sqrt{2\gamma_c}\hat{c}^{in}, \quad (3)$$

$$\frac{d\hat{m}}{dt} = -(i\Delta_m + \gamma_m)\hat{m} - ig_{mc}\hat{c} + \sqrt{2\gamma_m}\hat{m}^{in}. \quad (4)$$

The input quantum noise operators \hat{c}^{in} and \hat{m}^{in} are characterized by the correlation functions

$$\langle \hat{o}^{in}(t)\hat{o}^{in\dagger}(t') \rangle = (1 + \bar{n}_o)\delta(t - t'), \quad (5)$$

$$\langle \hat{o}^{in\dagger}(t)\hat{o}^{in}(t') \rangle = \bar{n}_o\delta(t - t'), \quad (6)$$

with \bar{n}_o (for $o = c, m$) representing the equilibrium thermal occupancy of the respective modes, defined by the Bose-Einstein distribution $\bar{n}_o = [\exp(\hbar\omega_o/k_B T) - 1]^{-1}$. Under the condition $\omega_c \simeq \omega_m$, which is typical for resonant microwave-magnon coupling, we adopt the approximation $\bar{n}_c \simeq \bar{n}_m \equiv \bar{n}$ for the mean thermal excitation numbers [26]. In the limit of a strong drive, the magnon mode acquires a large semi-classical mean field $|\langle \hat{m} \rangle| \gg 1$ at steady state, allowing for the standard linearization of the system dynamics. The beam-splitter coupling ensures that the large displacement of the magnon mode is transferred to the cavity field, such that $|\langle \hat{c} \rangle| \gg 1$. Consequently, we can linearize the dynamics by decomposing each operator into its steady-state mean value and a small quantum fluctuation, $\hat{o} = \langle \hat{o} \rangle + \delta\hat{o}$, while discarding second-order fluctuation terms. The steady-state values of the system operators written as

$$\langle \hat{c} \rangle = \frac{\epsilon_L \left((\Delta_m^2 + \gamma_m^2)(\gamma_c + 2\lambda \cos(\theta)) + g_{mc}^2 \gamma_m \right) + i\epsilon_L \left((\gamma_m^2 + \Delta_m^2)(2\lambda \sin(\theta) - \Delta_c) + g_{mc}^2 \Delta_m \right)}{\gamma_m \left(2g_{mc}^2 \gamma_c + \gamma_m (\Delta_c^2 - 4\lambda) + \gamma_c^2 \gamma_m \right) - 2g_{mc}^2 \Delta_c \Delta_m + \Delta_m^2 (\Delta_c^2 + \gamma_c^2 - 4\lambda) + g_{mc}^4}, \quad (7)$$

$$\langle \hat{m} \rangle = \frac{g_{mc}\epsilon_L (\gamma_m (\Delta_c - 2\lambda \sin(\theta)) + \Delta_m (\gamma_c + 2\lambda \cos(\theta))) + ig_{mc}\epsilon_L (\gamma_m (\gamma_c + 2\lambda \cos(\theta)) + \Delta_m (2\lambda \sin(\theta) - \Delta_c) + g_{mc}^2)}{\gamma_m \left(2g_{mc}^2 \gamma_c + \gamma_m (\Delta_c^2 - 4\lambda) + \gamma_c^2 \gamma_m \right) - 2g_{mc}^2 \Delta_c \Delta_m + \Delta_m^2 (\Delta_c^2 + \gamma_c^2 - 4\lambda) + g_{mc}^4}. \quad (8)$$

To analyze the fluctuation dynamics, we introduce the quadrature operators $\delta\hat{X}_c = (\delta\hat{c} + \delta\hat{c}^\dagger)/\sqrt{2}$, $\delta\hat{P}_c = i(\delta\hat{c}^\dagger - \delta\hat{c})/\sqrt{2}$, and similarly for the magnon mode. The resulting linearized QLEs for the quadrature vector $\mathbf{u}(t) = [\delta\hat{X}_c, \delta\hat{P}_c, \delta\hat{X}_m, \delta\hat{P}_m]^\top$ are written compactly as

$$\dot{\mathbf{u}}(t) = \mathcal{A}\mathbf{u}(t) + \mathbf{n}(t), \quad (9)$$

where $\mathbf{n}(t)$ is the input noise vector given by $\mathbf{n}(t) = [\sqrt{2\gamma_c}\hat{X}_c^{in}, \sqrt{2\gamma_c}\hat{P}_c^{in}, \sqrt{2\gamma_m}\hat{X}_m^{in}, \sqrt{2\gamma_m}\hat{P}_m^{in}]^\top$ and the drift matrix \mathcal{A} takes the form

$$\mathcal{A} = \begin{bmatrix} -\gamma_c + 2\lambda \cos(\theta) & \Delta_c + 2\lambda \sin(\theta) & 0 & g_{mc} \\ -\Delta_c + 2\lambda \sin(\theta) & -\gamma_c - 2\lambda \cos(\theta) & -g_{mc} & 0 \\ 0 & g_{mc} & -\gamma_m & \Delta_m \\ -g_{mc} & 0 & -\Delta_m & -\gamma_m \end{bmatrix}. \quad (10)$$

Taking into account the characteristic equation $\det(\mathcal{A} - \lambda\mathbb{I}) = \lambda^4 + f_1\lambda^3 + f_2\lambda^2 + f_3\lambda + f_4$. Based on the Routh–Hurwitz stability criterion [106], the system is stable if and only if all Hurwitz determinants are positive. Consequently, the stability of the system is ensured when the following conditions are satisfied:

$$\begin{aligned} f_1 &> 0, \\ f_1 f_2 - f_3 &> 0, \\ f_1 f_2 f_3 - f_1^2 f_4 - f_3^2 &> 0, \\ f_1 f_2 f_3 f_4 - f_1^2 f_4^2 - f_3^2 f_4 - f_4^2 &> 0. \end{aligned} \quad (11)$$

The linearized dynamics and Gaussian nature of the noise terms ensure that the steady-state fluctuations form a Gaussian state, characterized by the 4×4 covariance matrix C

$$C_{ij} = \frac{1}{2} \langle \mathbf{u}_i(t)\mathbf{u}_j(t') + \mathbf{u}_j(t')\mathbf{u}_i(t) \rangle \quad (i, j = 1, 2, \dots, 4). \quad (12)$$

The dynamics-state values of the covariance matrix are governed by the following Lyapunov equation [107, 108]

$$\partial_t \mathcal{C} = \mathcal{A}\mathcal{C} + \mathcal{C}\mathcal{A}^\top + \mathcal{D}, \quad (13)$$

where the diffusion matrix, determined by the noise correlations $\frac{1}{2}\langle \mathbf{n}_i(t)\mathbf{n}_j(t') + \mathbf{n}_j(t')\mathbf{n}_i(t) \rangle = \mathcal{D}_{ij}\delta(t - t')$, is given by $\mathcal{D} = \text{diag}[\gamma_c(2\bar{n}_c + 1), \gamma_c(2\bar{n}_c + 1), \gamma_m(2\bar{n}_m + 1), \gamma_m(2\bar{n}_m + 1)]$. Here, the system is taken to be initially in the vacuum state.

IV. QUANTUM AND CLASSICAL FISHER INFORMATION

A. Quantum multiparameter estimation in phase space

Multiparameter estimation constitutes a foundational problem within quantum estimation theory, extending the principles of single-parameter sensing to more complex systems. In a typical quantum estimation scheme, a probe is initialized and evolved through a channel encoded with the target parameters. By measuring the output state and applying an appropriate estimator, the values of the parameters are extracted. We consider a parameter-dependent family of quantum states ρ_ϵ , where $\epsilon = (\epsilon_1, \epsilon_2, \dots, \epsilon_d)$ denotes a vector of d physical parameters to be estimated. Moreover, the objective of quantum estimation is to determine ϵ through a measurement scheme $\{M_z\}$ and a corresponding estimator $\hat{\epsilon}(z)$. Here, the measurement is characterized by a set of POVM elements M_z that sum to the identity. The likelihood of obtaining a specific outcome z for a given parameter set ϵ is determined by the Born rule, $p(z|\epsilon) = \text{Tr}[\rho_\epsilon M_z]$. To quantify the sensitivity of the state to the parameters, we introduce the Symmetric Logarithmic Derivative (SLD) and Right Logarithmic Derivative (RLD) operators for each parameter ϵ_α , defined respectively by the following relations [109–114]

$$\partial_{\epsilon_\alpha} \varrho = (L_\alpha^{(S)} \varrho + \varrho L_\alpha^{(S)})/2 \quad (\text{SLD}). \quad (14)$$

$$\partial_{\epsilon_\alpha} \varrho = \varrho L_\alpha^{(R)} \quad (\text{RLD}). \quad (15)$$

Using the SLD and RLD operators, we define the corresponding quantum Fisher information matrices as follows

$$\mathbf{H}_{\alpha\beta} = \text{Tr} \left[\varrho_\epsilon \left(\frac{L_\alpha^{(S)} L_\beta^{(S)} + L_\beta^{(S)} L_\alpha^{(S)}}{2} \right) \right], \quad (16)$$

$$\mathbf{J}_{\alpha\beta} = \text{Tr}[\varrho_\epsilon L_\beta^{(R)} L_\alpha^{(R)\dagger}]. \quad (17)$$

The precision of the estimation is bounded by two different Cramér-Rao inequalities. Specifically, defining the outcome covariance matrix as $V(\epsilon)_{\alpha\beta} = \langle z_\alpha z_\beta \rangle - \langle z_\alpha \rangle \langle z_\beta \rangle$ and choosing a positive-definite weight matrix \mathbf{G} , we have

$$\text{Tr}[\mathbf{G}\mathbf{V}] \geq \text{Tr}[\mathbf{G}(\mathbf{H})^{-1}]/M, \quad (18)$$

$$\text{Tr}[\mathbf{G}\mathbf{V}] \geq \text{Tr}[\mathbf{G}\text{Re}(\mathbf{J}^{-1})] + \text{Tr}[\mathbf{G}\text{Im}(\mathbf{J}^{-1})]/M, \quad (19)$$

where $\text{Tr}[A]$ signifies the trace operation over the finite-dimensional space of matrix A , and M denotes the sample size or number of measurement repetitions. For the specific choice of $\mathbf{G} = \mathbb{I}$, these inequalities reduce to bounds on the sum of the variances of the estimated parameters.

$$\sum_\alpha \text{Var}(z_\alpha) \geq \mathbf{B}_S := \text{Tr}[\mathbf{H}^{-1}]/M, \quad (20)$$

$$\sum_\alpha \text{Var}(z_\alpha) \geq \mathbf{B}_R := \text{Tr}[\text{Re}(\mathbf{J}^{-1})] + \text{Tr}[\text{Im}(\mathbf{J}^{-1})]/M. \quad (21)$$

where we have decomposed the inverse of the Quantum Fisher Information Matrix into its real and imaginary parts, $\mathbf{F}^{-1} \equiv \mathbf{F}_R + i\mathbf{F}_I$, and utilized the operator absolute value $|A| \equiv \sqrt{\mathbf{A}\mathbf{A}^\dagger}$. As before, M denotes the total number of measurement trials. The matrices \mathbf{H} and \mathbf{J} are referred to as the SLD [115] and RLD [116–118] quantum Fisher information matrices, respectively. The attainability of the SLD and RLD bounds is generally restricted [119]. Due to quantum non-commutativity, it is often impossible to reach the precision limits for all parameters simultaneously, as the optimization of one measurement typically disturbs the estimation of the others. Furthermore, the optimal estimator associated with the RLD bound does not always correspond to a physically realizable POVM. Conversely, even when the optimal measurements for individual parameters are non-commuting, it may still be possible to saturate both bounds through the implementation of a joint measurement strategy. While much of the work in this field centers on the SLD bound [120–126], it is well established that for single-parameter estimation, the SLD QFI is smaller than the RLD QFI. This relationship ensures that the SLD approach provides the tighter bound for sensitivity [110, 127].

Furthermore, while the single-parameter SLD bound is asymptotically attainable in the limit of large M , the multiparameter case is more constrained. Recent developments in quantum local asymptotic normality suggest that the bound in Eq. (18) is asymptotically saturable if and only if the weak compatibility condition is satisfied [120]: $\text{Tr}[\varrho[\mathbf{L}_i, \mathbf{L}_j]] = 0$. In scenarios where this condition is violated, the RLD bound may provide a more stringent limit, thereby assuming greater significance for characterizing the system's precision.

It is therefore essential to identify the conditions under which these inequalities are saturated in multiparameter scenarios, enabling the realization of an optimal measurement strategy. In this regard, it is worth noting that while several studies in quantum multiparameter estimation theory [128–131] have focused on the SLD-based framework, they predominantly demonstrate that the Quantum Cramér-Rao Bounds (QCRBs) in Eqs. (18) and (20) are saturable if and only if

$$\text{Tr}[\varrho[\mathbf{L}_{\epsilon_\alpha}^{(S)}, \mathbf{L}_{\epsilon_\beta}^{(S)}]] = 0. \quad (22)$$

It is straightforward to show that condition (22) can be reformulated as

$$\text{Im}(\text{Tr}[\varrho[\mathbf{L}_{\epsilon_\alpha}^{(S)}, \mathbf{L}_{\epsilon_\beta}^{(S)}]]) = 0. \quad (23)$$

It is therefore pertinent to explore the link between the RLD and SLD bounds to identify which is more fundamental. This led to the development of the most informative QCRB (B_{MI}) [114, 132], defined as follows

$$B_{MI} = \min\{B_R, B_S\}. \quad (24)$$

Accordingly, the most informative QCRB is determined by comparing the SLD and RLD limits. We thus define the following ratio

$$\mathcal{R} = \frac{B_S}{B_R}, \quad (25)$$

Depending on the ratio \mathcal{R} , B_{MI} takes the following values

$$B_{MI} = \begin{cases} B_S & \text{if } \mathcal{R} < 1, \\ B_R & \text{if } \mathcal{R} > 1, \end{cases}$$

naturally, if $\mathcal{R} = 1$, then $B_{MI} = B_R = B_S$.

In summary, the optimal precision limits in the multiparameter regime can be unified into a single inequality, expressed as

$$\sum_{\alpha}^N \text{var}[\epsilon_{\alpha}] \geq \frac{B_{MI}}{M}. \quad (26)$$

The SLD and RLD quantum Fisher information matrices are derived in detail in [112, 132]. Specifically, provided that $\Gamma = 2C + i\Omega$ is invertible, the RLD matrix can be expressed as

$$\mathbf{J}_{\epsilon_\alpha \epsilon_\beta} = 2\text{vec}[\partial_{\epsilon_\alpha} C]^\dagger \Sigma^{-1} \text{vec}[\partial_{\epsilon_\beta} C] + 2\partial_{\theta_\mu} \mathbf{d}^\top \Gamma^{-1} \partial_{\theta_\nu} \mathbf{d}. \quad (27)$$

Under this condition, the Moore-Penrose pseudoinverse of Γ reduces to its standard inverse, with $\Sigma = \Gamma^\dagger \oplus \Gamma$. The components of the SLD quantum Fisher information matrix are given by [109, 110, 112]

$$\mathbf{H}_{\epsilon_\alpha \epsilon_\beta} = 2\text{vec}[\partial_{\epsilon_\alpha} C]^\dagger \mathcal{M}^\dagger \text{vec}[\partial_{\epsilon_\beta} C] + \partial_{\epsilon_\alpha} \mathbf{d}^\top C^{-1} \partial_{\epsilon_\beta} \mathbf{d}. \quad (28)$$

with $\mathcal{M} = 4C^\dagger \otimes C + \Omega \otimes \Omega$, where $\Omega = \begin{bmatrix} 0 & 1 \\ -1 & 0 \end{bmatrix} \oplus \begin{bmatrix} 0 & 1 \\ -1 & 0 \end{bmatrix}$. Provided that \mathcal{M} is invertible, the SLD quantum Fisher information matrix can be expressed as

$$\mathbf{H}_{\epsilon_\alpha \epsilon_\beta} = 2\text{vec}[\partial_{\epsilon_\alpha} C]^\dagger \mathcal{M}^{-1} \text{vec}[\partial_{\epsilon_\beta} C] + \partial_{\epsilon_\alpha} \mathbf{d}^\top C^{-1} \partial_{\epsilon_\beta} \mathbf{d}. \quad (29)$$

Thus, for the estimation of the parameters: the cavity-magnon coupling g_{mc} or dissipation rate of cavity mode γ_c with $\mathbf{d} = [\langle \hat{X}_c \rangle, \langle \hat{P}_c \rangle, \langle \hat{X}_m \rangle, \langle \hat{P}_m \rangle]^\top$, the RLD quantum Fisher information matrix \mathbf{J} , can be calculated from Eq. (27), as

$$\mathbf{J} = \begin{pmatrix} 2\text{vec}[\partial_{g_{mc}} C]^\dagger \Sigma^{-1} \text{vec}[\partial_{g_{mc}} C] + 2\partial_{g_{mc}} \mathbf{d}^\top \Gamma^{-1} \partial_{g_{mc}} \mathbf{d} & 2\text{vec}[\partial_{g_{mc}} C]^\dagger \Sigma^{-1} \text{vec}[\partial_{\gamma_c} C] + 2\partial_{g_{mc}} \mathbf{d}^\top \Gamma^{-1} \partial_{\gamma_c} \mathbf{d} \\ 2\text{vec}[\partial_{\gamma_c} C]^\dagger \Sigma^{-1} \text{vec}[\partial_{g_{mc}} C] + 2\partial_{\gamma_c} \mathbf{d}^\top \Gamma^{-1} \partial_{g_{mc}} \mathbf{d} & 2\text{vec}[\partial_{\gamma_c} C]^\dagger \Sigma^{-1} \text{vec}[\partial_{\gamma_c} C] + 2\partial_{\gamma_c} \mathbf{d}^\top \Gamma^{-1} \partial_{\gamma_c} \mathbf{d} \end{pmatrix}, \quad (30)$$

the SLD quantum Fisher information matrix \mathbf{H} , can be calculated from Eq. (29), as

$$\mathbf{H} = \begin{pmatrix} 2\text{vec}[\partial_{g_{mc}} C]^\dagger \mathcal{M}^{-1} \text{vec}[\partial_{g_{mc}} C] + \partial_{g_{mc}} \mathbf{d}^\top C^{-1} \partial_{g_{mc}} \mathbf{d} & 2\text{vec}[\partial_{g_{mc}} C]^\dagger \mathcal{M}^{-1} \text{vec}[\partial_{\gamma_c} C] + \partial_{g_{mc}} \mathbf{d}^\top C^{-1} \partial_{\gamma_c} \mathbf{d} \\ 2\text{vec}[\partial_{\gamma_c} C]^\dagger \mathcal{M}^{-1} \text{vec}[\partial_{g_{mc}} C] + \partial_{\gamma_c} \mathbf{d}^\top C^{-1} \partial_{g_{mc}} \mathbf{d} & 2\text{vec}[\partial_{\gamma_c} C]^\dagger \mathcal{M}^{-1} \text{vec}[\partial_{\gamma_c} C] + \partial_{\gamma_c} \mathbf{d}^\top C^{-1} \partial_{\gamma_c} \mathbf{d} \end{pmatrix}. \quad (31)$$

Then, B_S can be calculated from Eqs. (20) and (30), and B_R from Eqs. (21) and (31).

B. Classical Fisher information for Gaussian states : Heterodyne

This section details the Classical Fisher Information (CFI) framework. In this context, a quantum measurement is described by a Positive-Operator Valued Measure (POVM) $\{\hat{\Pi}_z\}$, where each operator is positive semi-definite ($\hat{\Pi}_y \geq 0$) and the set satisfies the completeness condition $\sum_z \hat{\Pi}_z = \mathbb{I}$ [133]. We denote the set of all such valid measurement schemes as $\tilde{\Omega}$. The measurement outcomes are characterized by a conditional probability distribution determined by the Born rule

$$\{P(z|\epsilon) = \text{Tr}[\mathcal{Q}_\epsilon \hat{\Pi}_z]\}, \quad (32)$$

with $P(z|\epsilon)$ denoting the conditional probability for the measurement result z . From this distribution, the value of the parameter ϵ can be estimated, with the CFI defined as [115, 134, 135]

$$F_\epsilon = \int \frac{1}{P(z|\epsilon)} \left[\frac{\partial P(z|\epsilon)}{\partial \epsilon} \right]^2 dz. \quad (33)$$

Since the QFI is defined as $H_\epsilon := \max_{\tilde{\Omega}} \{F_\epsilon\}$, it inherently accounts for the optimal measurement strategy. Thus, we obtain

$$\text{Var}(\hat{\epsilon}) \geq \frac{1}{MF_\epsilon} \geq \frac{1}{M H_\epsilon}. \quad (34)$$

The lower bound of the classical CRB is achievable through optimal estimation strategies; for instance, the maximum likelihood estimator is known to be asymptotically efficient. It should be noted that all measurements considered in this work are assumed to be ideal, corresponding to a measurement efficiency of unity. The calculation of the CFI is performed using the second-moment matrix C and the first-moment vector \mathbf{d} .

Heterodyne detection.—An essential Gaussian measurement technique is heterodyne detection, which involves mixing the measured field with a probe field of a different frequency. The corresponding measurement operators are defined by the over-complete set of coherent state projectors, $\{|\alpha\rangle\langle\alpha|\}/\pi$, which constitute a valid POVM [95, 96, 127, 136]. The heterodyne detection scheme typically involves mixing the mode of interest with an ancillary vacuum state via a 50 : 50 beam splitter. The Q and P quadratures of the resulting modes are then measured. For the cavity-magnon system, the realization of optimal heterodyne detection on its subsystems is described in [137]

$$F_{\epsilon, \text{Het}} = \frac{1}{2} \text{Tr} \left(\sigma^{-1} \frac{d\sigma_\Lambda}{d\epsilon} \sigma^{-1} \frac{d\sigma}{d\epsilon} \right) + \frac{d\mathbf{d}^\top}{d\epsilon} \sigma^{-1} \frac{d\mathbf{d}}{d\epsilon}, \quad (35)$$

where $\sigma = C + \mathbb{I}_{4 \times 4}$, and the subscript ‘‘Het’’ marks the heterodyne detection.. Here, \mathbf{d} and C are the first and second moments of the bipartite system, while $\mathbb{I}_{4 \times 4}$ represents the supplemental noise inherent in the simultaneous measurement of conjugate quadratures Q and P .

Homodyne detection.—In homodyne detection, the signal and a strong local oscillator are mixed at the same frequency, resulting in a measurement of a single quadrature. The corresponding POVM elements are $\{|Q\rangle\langle Q|\}$ or $\{|P\rangle\langle P|\}$, representing the eigenstates of the Q or P quadrature [95, 96, 127, 136]. Moreover, $Q \in \{\hat{X}_c, \hat{X}_m\}$ and $P \in \{\hat{Y}_c, \hat{Y}_m\}$, the cavity quadratures are directly measurable, whereas the magnon quadratures are detected via auxiliary fields. This is typically implemented by coupling the YIG sphere to a weakly driven microwave cavity. Under homodyne detection, the CFI with respect to ϵ can be expressed as follows [138]

$$F_{\epsilon, \text{Ho}}^j = \frac{1}{2C_{jj}^2} \left[2C_{jj} (\partial_\epsilon \mathbf{d}_j)^2 + (\partial_\epsilon C_{jj})^2 \right], \quad (36)$$

where, the superscript ‘‘ j ’’ labels the measured quadrature, while the subscript ‘‘Ho’’ refers to homodyne detection. Specifically, the CFI for parameters such as the cavity-magnon coupling g_{mc} or dissipation rate of cavity mode γ_c , utilizing homodyne measurements of $d_1 = \langle \hat{X}_c \rangle$ and $d_2 = \langle \hat{Y}_c \rangle$, are expressed as

$$F_{g, \text{Ho}}^{\hat{X}_c} = \frac{1}{2C_{11}^2} \left[2C_{11} (\partial_g \langle \hat{X}_c \rangle)^2 + (\partial_g C_{11})^2 \right], \quad F_{\gamma_c, \text{Ho}}^{\hat{X}_c} = \frac{1}{2C_{11}^2} \left[2C_{11} (\partial_{\gamma_c} \langle \hat{X}_c \rangle)^2 + (\partial_{\gamma_c} C_{11})^2 \right], \quad (37)$$

and

$$F_{g, \text{Ho}}^{\hat{Y}_c} = \frac{1}{2C_{22}^2} \left[2C_{22} (\partial_g \langle \hat{Y}_c \rangle)^2 + (\partial_g C_{22})^2 \right], \quad F_{\gamma_c, \text{Ho}}^{\hat{Y}_c} = \frac{1}{2C_{22}^2} \left[2C_{22} (\partial_{\gamma_c} \langle \hat{Y}_c \rangle)^2 + (\partial_{\gamma_c} C_{22})^2 \right]. \quad (38)$$

V. RESULTS AND DISCUSSIONS

We now examine the sensitivity of the estimation precision for the coupling strength g_{mc} and cavity decay γ_c to several system parameters in steady and dynamical state. These include the environmental temperature T , driving power P , and the respective dissipation rates and detunings of the cavity and magnon modes ($\gamma_{c,m}$ and $\Delta_{c,m}$). Moreover, the effects of the OPA parameters, namely the gain λ and squeeze phase θ , are considered. Additionally, we compare the SLD-optimized quantum bound with the CFI results achieved under heterodyne and homodyne detection. Besides, the feasible value of the parameters reported in [19, 21, 23, 52]: $P = 500$ mW, $\omega_L/2\pi = 10$ GHz, $T = 10$ mK, $\gamma_c/2\pi = 5$ MHz, $\gamma_m/2\pi = 40$ MHz, $\Delta_c/2\pi = 40$ MHz, $\Delta_m = 0$, $g_{mc}/2\pi = 41$ MHz.

A. Steady-state

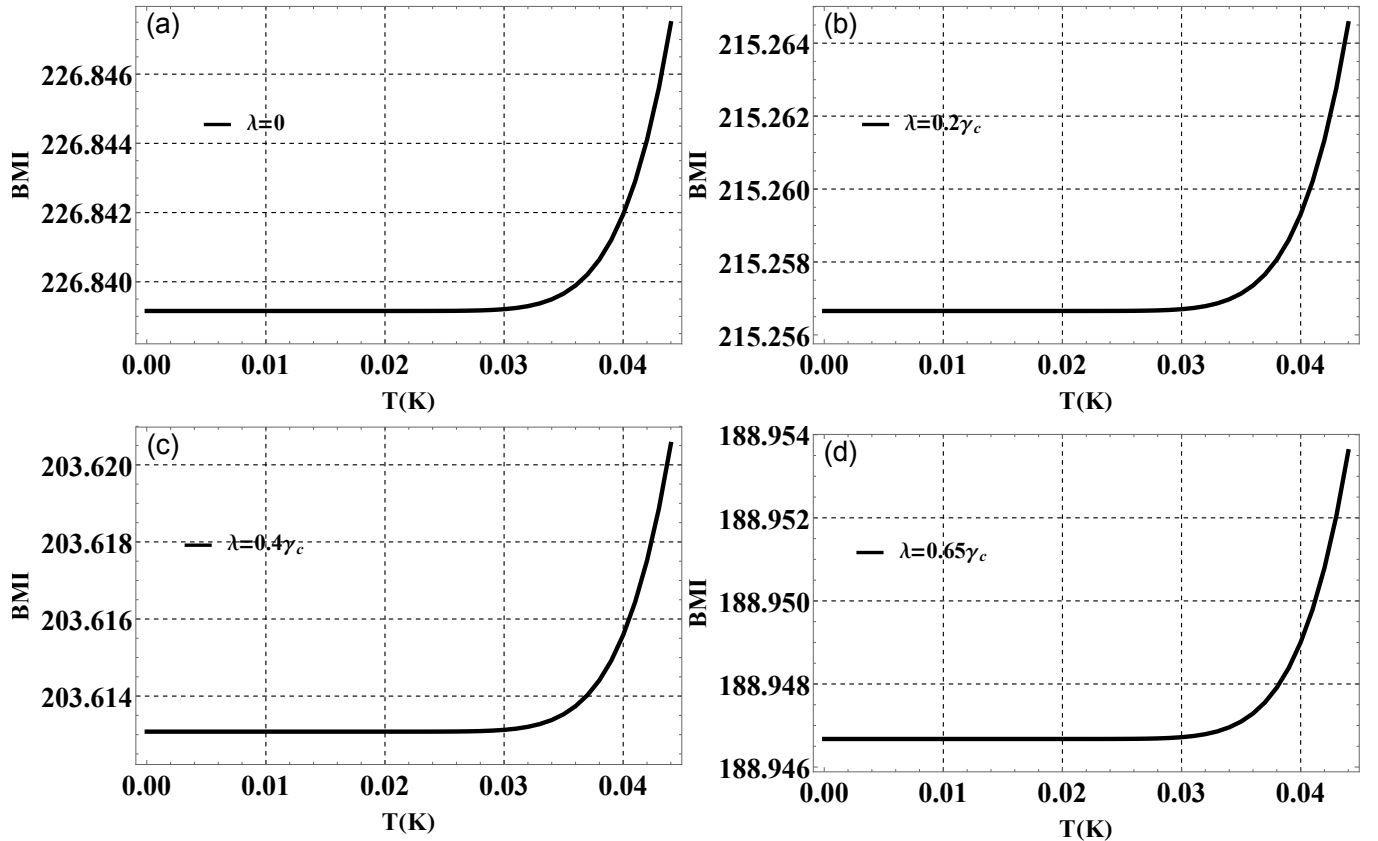


FIG. 2. Plot of the BMI as function of the temperature T for different values of the gain λ , with $\theta = 1.65\pi$.

To gain further insight into the effect of various OPA gain values, λ , on the most informative quantum Cramér-Rao Bound (BMI QCRB), Fig. 2 illustrates the BMI as a function of temperature T for different values of the OPA gain λ . One can see that for $\lambda = 0$ (absence of OPA), the BMI increases monotonically with increasing temperature, as depicted in Fig. 2(a). This behavior indicates a degradation of the multiparameter estimation precision due to the enhancement of thermal noise. One can see that when the value of the gain λ is increased, a significant diminishing of the BMI is achieved for a wide range of temperature in comparing with the case when $\lambda = 0$, as shown in Figs. 2(a-d). This demonstrates that the presence of an OPA effectively enhances the precision of multiparameter estimation. Moreover, the degradation of estimation precision is mitigated due to the strong suppression of thermal noises provided by the OPA. This can also be explained by the generation of squeezed light via the OPA, which leads to a reduction in the BMI values over a wide temperature range, as shown in Fig. 2(a). Nevertheless, despite this improvement, the BMI still increases monotonically with temperature T . This rise occurs once the temperature exceeds a threshold of approximately 0.03 K, confirming that thermal effects continue to negatively impact estimation performance even in the presence of an OPA.

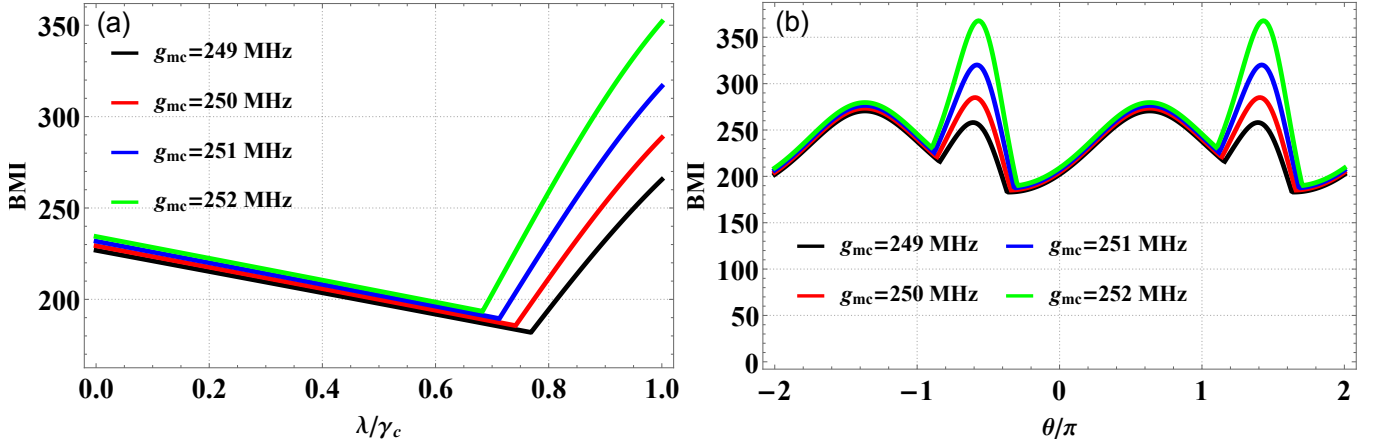


FIG. 3. Plot of the variation of the BMI versus (a) λ/γ_c with $\theta = 1.65\pi$ and (b) θ/π with $\lambda = 0.75\gamma_c$, for different values of g_{mc} .

Figure 3 shows the behavior of the BMI as a function of (a) the normalized gain λ/γ_c and (b) the phase θ/π for various values of the cavity-magnon coupling strength g_{mc} . In Fig. 3(a), we observe that the BMI decreases as the parameter λ increases. This reduction in the BMI QCRB indicates an enhancement in estimation precision. This means, the inclusion of an OPA enhances robustness against strong coupling g_{mc} , thereby improving the precision of multiparameter estimation. However, once λ exceeds approximately $0.7\gamma_c$, the BMI begins to increase almost linearly. Moreover, increasing the coupling rate g_{mc} leads to a higher BMI QCRB, as illustrated in Fig. 3(a). This implies that stronger coupling reduces the available information and therefore lowers the estimation precision. In Fig. 3(b), the BMI exhibits a periodic dependence on the phase θ/π , reaching its maximum at phase $\theta = (2n + 1.6)\pi$ ($n \in \mathbb{Z}$), and its minimum at $\theta = (2n + 1.2)\pi$. The magnon-photon coupling g_{mc} also affects this behavior by increasing the minimum BMI QCRB value, which corresponds to a further degradation in precision. Overall, the gain λ , the phase θ , and the coupling strength g_{mc} all play crucial roles in modulating the amount of extractable information in the system.

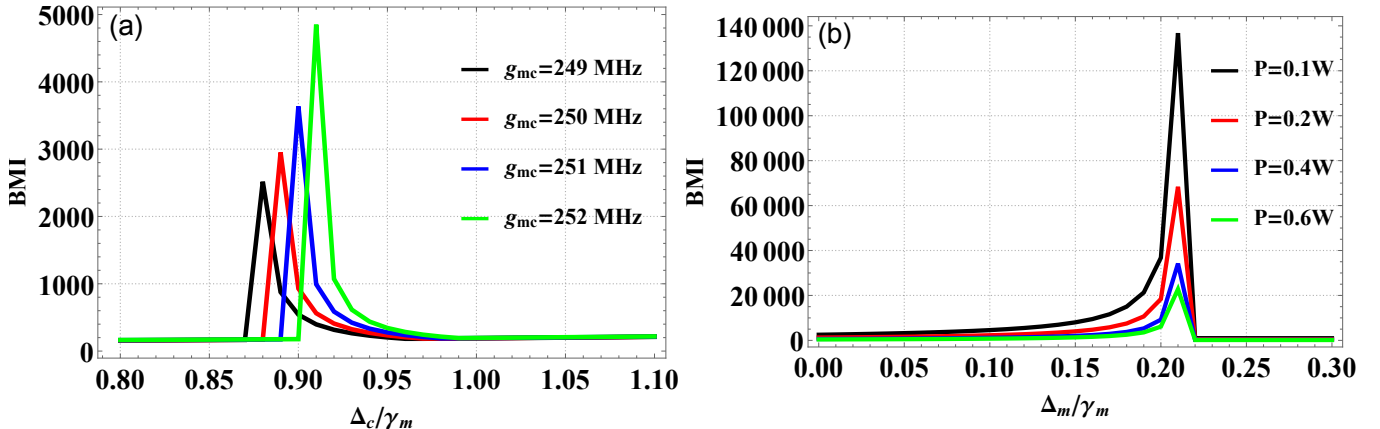


FIG. 4. Plot of the variation of the BMI as function of (a) cavity detuning Δ_c/γ_m for different value of the cavity-magnon coupling g_{mc} and (b) magnon detuning Δ_m/γ_m for different value of the power P . Using $\lambda = 0.67\gamma_c$ and $\theta = 1.65\pi$.

Figure 4 shows the behavior of the BMI QCRB as a function of the cavity detuning Δ_c/γ_m in the steady state. As seen in Fig. 4(a), for small values of cavity detuning, the QCRB is small compared to its maximum value. A small BMI value indicates, in principle, an estimation with high precision. When the cavity detuning exceeds approximately $0.85\gamma_c$, the QCRB begins to increase significantly, signaling a degradation in estimation precision due to off-resonance effects. Consistent with the behavior observed in Fig. 3, increasing the cavity-magnon coupling strength g_{mc} leads to a higher QCRB, resulting in lower estimation precision. Furthermore, when g_{mc} is reduced, the onset of QCRB growth occurs at smaller values of cavity detuning, showing that weaker coupling makes the estimation more sensitive to detuning variations.

In Fig. 4(b), we plot the BMI as a function of the magnon detuning Δ_m/γ_m for different values of the driving power P . For small detuning values, the BMI remains low, which again indicates a region of high precision for multiparameter estimation. As Δ_m increases beyond $0.15\gamma_m$, the BMI increases rapidly toward its maximum, marking a reduction in precision. Interestingly, for

$\Delta_m > 0.25\gamma_c$, the BMI returns to small values, implying another region of enhanced precision. Finally, increasing the power P contributes to improving the multiparameter estimation precision, as it generally reduces the maximum value of the BMI across the entire detuning range.

B. Dynamical state

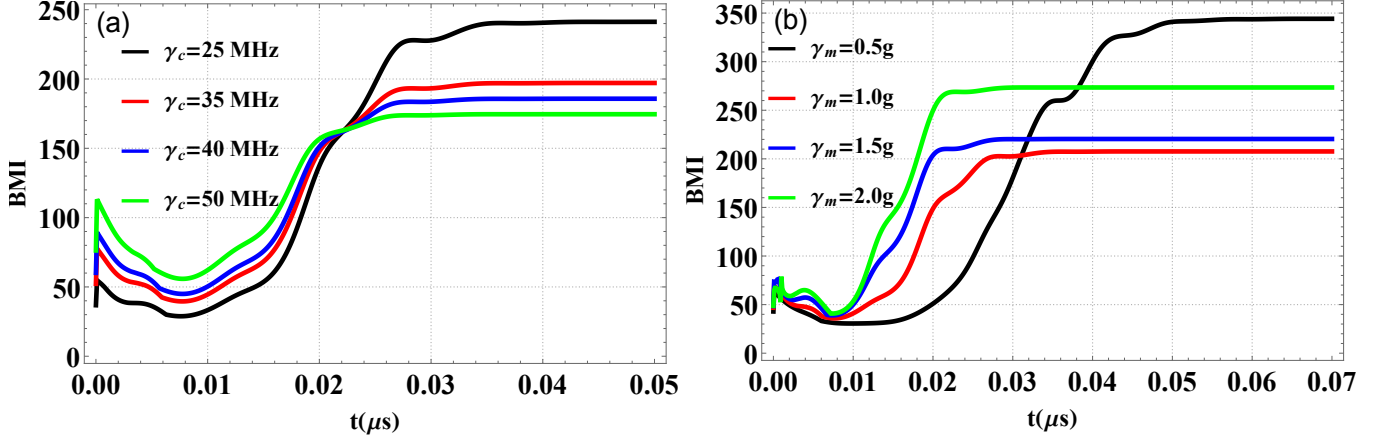


FIG. 5. Plot of the dynamical evolution of the BMI for various value of (a) γ_c and (b) γ_m/g_{mc} with $\lambda = 0.65\gamma_c$ and $\theta = 1.65\pi$.

In Fig. 5(a), we plot the BMI as a function of time for different values of the cavity decay rate γ_c . At very short times, the BMI decreases with increasing γ_c when approximately $t < 7$ ns, indicating an initial enhancement of the multiparameter estimation precision. Furthermore, when the time exceeds approximately $t > 0.01 \mu\text{s}$, the BMI begins to grow significantly to achieve its steady-state around $\text{BMI} \approx 200$. Besides, when $\gamma_c = 25 \text{ MHz}$, the BMI remains relatively low initially but starts increasing once $t > 0.02 \mu\text{s}$, highlighting the effect of cavity losses on long-time estimation performance. Moreover, as γ_c increases, the BMI becomes larger throughout the dynamical evolution, which means that stronger cavity dissipation degrades the precision of parameter estimation when approximately $t > 0.022 \mu\text{s}$.

Figure 5(b) explores the dynamical evolution of the BMI for various values of γ_m . At early times ($t < 0.01 \mu\text{s}$), the BMI decreases, revealing a short interval of improved multiparameter estimation precision. However, beyond this point, all curves exhibit an exponential rise in the BMI, indicating a rapid loss of precision as γ_m drives the dynamics for $t < 0.038 \mu\text{s}$. For $t > 0.038 \mu\text{s}$, the BMI reaches its steady state, where it increases with γ_m , as depicted in Fig. 5(b).

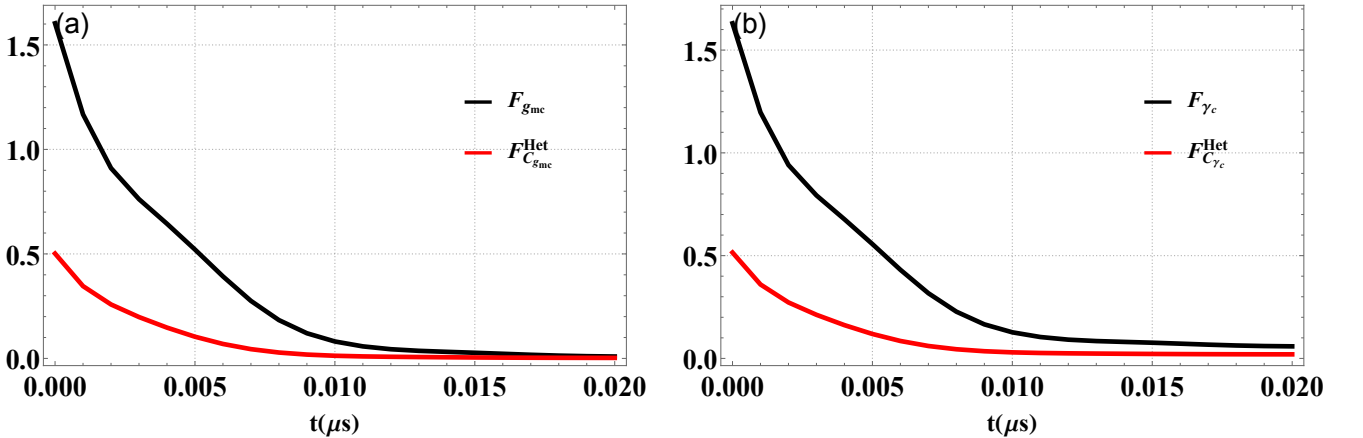


FIG. 6. Dynamical evolution of the SLD QFI (red curve) and the CFI in heterodyne detection, in (a) H_{gmc} and $F_{C_{gmc}}^{\text{Het}}$; in (b) H_{γ_c} and $F_{C_{\gamma_c}}^{\text{Het}}$. With $\lambda = 0.65\gamma_c$ and $\theta = 1.65\pi$.

To assess the sensitivity of g_{mc} and γ_c over time, we compare the ultimate quantum estimation (QFI) with the classical information (CFI) accessible via heterodyne detection. One can see that as the beginning of the evolution, the SLD QFI is significantly larger than the CFI, indicating that the quantum state contains considerably more information than what can be

accessed through classical measurements, as depicted in (a)-(b). Moreover, it is evident that as time progresses, both the SLD QFI and the CFI decrease. This indicates a degradation of the quantum estimation precision for g_{mc} and γ_c . Furthermore, the decline in the CFI reflects a corresponding loss of classical estimation accuracy. For times exceeding $t > 0.02 \mu s$, the QFI $H_{g_{mc}}$ and CFI $F_{C_{g_{mc}}}^{Het}$ become equal and converge to zero, as shown in (a). This indicates that no quantum advantage remains and that precise parameter estimation becomes effectively impossible in this region. However, in Fig. V B(b), quantum estimation precision for γ_c still exists, even if it is very small compared to its initial value of $H_{\gamma_c} \approx 1.7$ at $t \approx 0$ s; eventually, H_{γ_c} reaches a steady state of approximately 0.1. Apparently, the classical information $F_{C_{\gamma_c}}^{Het}$ is very small with respect to H_{γ_c} when $t > 0.01 \mu s$.

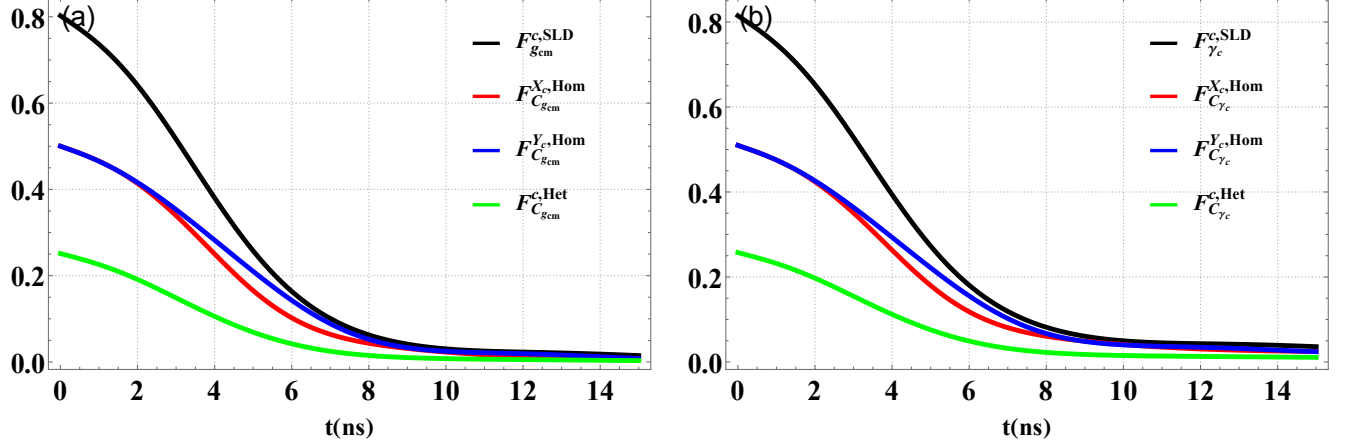


FIG. 7. Time evolution of the SLD QFI for the cavity mode (c) $F_{\epsilon}^{c,SLD}$ and the CFI in homodyne detection $F_{\epsilon}^{X_c,Hom}$ and $F_{\epsilon}^{Y_c,Hom}$, for quadrature operators X_c and Y_c , and in heterodyne detection $F_{\epsilon}^{c,Het}$, with $\epsilon = g_{mc}$ in (a) and $\epsilon = \gamma_c$ in (b), using $\lambda = 0.65\gamma_c$ and $\theta = 1.65\pi$.

Let us now compare the SLD QFI and the CFI for both homodyne and heterodyne detection of the cavity mode (c). As seen in Figs. 7(a) and (b), the CFI is bounded by the SLD QFI, indicating that the QFI provides higher precision than the CFI. Moreover, as shown in these figures, the QFI decreases monotonically over time, indicating that the quantum precision for estimating g_{mc} and γ_c degrades. We observe that for approximately $t \in [0, 3 \text{ ns}]$, the two homodyne CFIs are equal, satisfying $F_{g_{mc}}^{X_c,Hom} = F_{g_{mc}}^{Y_c,Hom}$. In the intermediate regime ($3 \text{ ns} < t < 8 \text{ ns}$), the hierarchy $F_{g_{mc}}^{Y_c,Hom} < F_{g_{mc}}^{X_c,Hom}$ emerges, showing that the X_c -quadrature becomes more informative than the Y_c -quadrature. Furthermore, for sufficiently long times ($t > 12 \text{ ns}$), both the SLD QFI and the CFI decay to zero, indicating a complete loss of information regarding the parameter g_{mc} , as depicted in Fig. 7(a).

A similar behavior is observed for the SLD QFI and CFI in the estimation of the cavity decay rate γ_c , as shown in Fig. 7(b). However, at long times, only the heterodyne CFI $F_{\gamma_c}^{c,Het}$ vanishes completely, whereas the homodyne CFIs retain small but nonzero values; this highlights the lower sensitivity of heterodyne detection to cavity dissipation in the long-time limit. Furthermore, a comparison between Figs. 7(a) and (b) reveals that $F_{g_{mc}}^{c,SLD} < F_{\gamma_c}^{c,SLD}$, meaning that the estimation precision for γ_c is higher than that for g_{mc} .

VI. CONCLUSION

In summary, we have proposed a theoretical scheme to enhance multiparameter quantum estimation in a feasible cavity-magnon system by incorporating a degenerate optical parametric amplifier (OPA). We have utilized the most informative quantum Cramér-Rao bound to evaluate the estimation performance, employing both the RLD and SLD operators. Besides, we have shown that the presence of the optical parametric amplifier significantly enhances estimation precision by reducing the BMI. This improvement arises from noise suppression facilitated by the OPA. Furthermore, we have discussed the effects of various physical parameters on the BMI in the steady state. We have used the Gaussian measurement schemes that can be realized experimentally. Moreover, we compared the CFI for heterodyne and homodyne detection with the SLD QFI, showing that these measurement schemes offer efficient and experimentally accessible strategies for parameter estimation.

[1] A. Ferraro, et al. arXiv. pre. quant-ph/0503237 16, 219 (2005).
 [2] S. Braunstein, P. Van Loock, Rev. mod. phys. 77, 513 (2005).
 [3] M. Kim, J. Lee, W. Munro, Phys. Rev. A, 66, 030301 (2002).
 [4] D. Vitali, et al. Phys. Rev. Lett. 98.3, 030405 (2007).

- [5] M. Paternostro, et al. *Phys. Rev. Lett.* 99.25 250401 (2007).
- [6] L. Tian, H. Wang, *Rev. Phys. A.* 82, 053806 (2010).
- [7] S. Gröblacher, et al. *Nature (London)* 460, 724 (2009).
- [8] J. D. Teufel, et al. *Nature (London)* 475, 359 (2011).
- [9] J. Chan, et al. *Nature (London)* 478, 89 (2011).
- [10] S. Olivares, et al. *Phys. Lett. A.* 319, 32-43 (2003).
- [11] X. Zhang, et al. *Sci. Adv.* 2, e1501286 (2016).
- [12] J. Li, et al. *Phys. Rev. Lett.* 121.20 203601 (2018).
- [13] P. G. Kevrekidis, et al. *Phys. Rev. Lett.* 90, 230401 (2003).
- [14] C. Gross, et al. *Nat.* 480, 219 (2011).
- [15] A. C. J. Wade, et al. *Phys. Rev. A.* 93, 023610 (2016).
- [16] J. Aasi, et al. *Nat. Photonics* 7, 613 (2013).
- [17] D. Wagle, et al. *J. Phys. Mater.* 7.2, 025005 (2024).
- [18] Y. Tabuchi, et al. *Phys. Rev. Lett.* 113.8, 083603 (2014).
- [19] X. Zhang, et al. *Phys. Rev. Lett.* 113.15, 156401 (2014).
- [20] I. L. S. Andrade, et al. *arXiv preprint arXiv:2508.02946* (2025).
- [21] M. S. Ebrahimi, et al. *Phys. Rev. A.* 103.6, 062605 (2021).
- [22] D. Xu, et al. *Phys. Rev. Lett.* 130.19, 193603 (2023).
- [23] J. X. Peng, et al. *Chaos, Solitons Fractals* 200, 117118 (2025).
- [24] H.Y. Yuan, et al. *Phys. Rep.* 1, 965 (2022).
- [25] Y. Tabuchi, et al. *Phys. Rev. Lett.* 113, 083603 (2014).
- [26] X. Zhang, et al. *Phys. Rev. Lett.* 113, 156401 (2014).
- [27] M. Goryachev, et al. *Phys. Rev. Applied.* 2, 054002 (2014).
- [28] T. Liu, et al. *Phys. Rev. B.* 94, 060405(R) (2016).
- [29] S. V. Kusminskiy, et al. *Phys. Rev. A.* 94, 033821 (2016).
- [30] S. Sharma, et al. *Phys. Rev. B.* 96, 094412 (2017).
- [31] X. Zhang, et al. *Phys. Rev. lett.* 117, 123605 (2016).
- [32] A. Osada, et al. *Phys. Rev. lett.* 116, 223601 (2016).
- [33] A. V. Chumak, et al. *Nat. Phys.* 11, 453-461 (2015).
- [34] S. P. Wolski, et al. *Phys. Rev. Lett.* 125.117701 (2020).
- [35] D. Zhang, et al. *npj Quantum Inf.* 1, 1 (2015).
- [36] H. Huebl, et al. *Phys. Rev. Lett.* 111, 127003 (2013).
- [37] X. Zhang, et al. *Sci. Adv.* 2, e1501286 (2016).
- [38] C. A. Potts, et al. *Phys. Rev. X.* 11.3, 031053 (2021).
- [39] R. Hisatomi, et al. *Phys. Rev. B.* 93, 174427 (2016).
- [40] J. Li, et al. *Phys. Rev. Lett.* 121, 203601 (2018).
- [41] M. Yu, et al. *Phys. Rev. Lett.* 124, 213604 (2020).
- [42] M. Yu, et al. *J. Phys. B: At. Mol. Opt. Phys.* 53, 065402 (2020).
- [43] J. Li, S. Gröblacher, *Quant. Sci. Technol.* 6, 024005 (2021).
- [44] J. Li, S.-Y. Zhu, *New J. Phys.* 21, 085001 (2019).
- [45] J. M. P. Nair, G. S. Agarwal, *arXiv preprint arXiv:1905.07884* (2019).
- [46] Z. Zhang, et al. *Phys. Rev. Research*, 1, 023021 (2019).
- [47] H. Tan, J. Li, *Phys. Rev. Research*, 3, 013192 (2021).
- [48] F. Bemani, et al. *Phys. Rev. A.* 99.6, 063814 (2019).
- [49] B. Hussain, et al. *Phys. Rev. A.* 105.6, 063704 (2022).
- [50] M. Amazioug, et al. *Entropy* 25.10, 1462 (2023).
- [51] M. Amazioug, et al. *Ann. Phys.* 537.12, e00289 (2025).
- [52] X. Deng, et al. *Phys. Rev. A.* 110.6, 063711 (2024).
- [53] J. Li, et al. *Natl. Sci. Rev.* 10.5, nwac247 (2023). XXX
- [54] J. Li, et al. *Phys. Rev. A.* 99, 02180(R) (2019).
- [55] M.-S. Ding, et al. *Sci. Rep.* 9, 1 (2019).
- [56] C. Potts, et al. *Phys. Rev. Applied.* 13, 064001 (2020).
- [57] N. Crescini, et al. *Appl. Phys. Lett.* 117, 144001 (2020).
- [58] N. Crescini, et al. *Phys. Rev. Appl.* 16(3), 034036 (2021).
- [59] Y. Cao, P. Yan, *Phys. Rev. B.* 99, 214415 (2019).
- [60] Z.-X. Liu, H. Xiong, and Y. Wu, *Phys. Rev. B.* 100, 134421 (2019).
- [61] J.-k. Xie, S.-l. Ma, and F.-l. Li, *Phys. Rev. A.* 101, 042331 (2020).
- [62] Q. Cai, J. Liao, B. Shen, G. Guo, and Q. Zhou, *arXiv:2011.04301*.
- [63] S.-f. Qi, J. Jing, *Phys. Rev. A.* 103, 043704 (2021).
- [64] B. Sarma, et al. *New J. Phys.* 23, 043041 (2021).
- [65] Y. J. Zhu, et al. *Adv. Quant. Technol.* 8.10, e2500148 (2025).
- [66] A. Holevo, *Probabilistic and Statistical Aspects of Quantum Theory* (Springer Berlin Heidelberg, 2011).
- [67] C. Helstrom, *Phys. Lett. A.* 25, 101 (1967).
- [68] C. W. Helstrom, *Quantum detection and estimation theory*, Vol. 123 (Academic press, 1976).

[69] D. Bures, *Trans. Amer. Math. Soc.* 135, 199 (1969).

[70] S. L. Braunstein, C. M. Caves, *Phys. Rev. Lett.* 72, 3439 (1994).

[71] M. G. A. Paris, *Int. J. Quantum Inf.* 07, 125 (2009).

[72] M. Szczykulska, et al. *Adv. Phys. X*, 1, 621 (2016).

[73] V. Giovannetti, et al. *Scien.* 306, 1330 (2004).

[74] M. Zwierz, et al. *Phys. Rev. Lett.* 105, 180402 (2010).

[75] V. Giovannetti, et al. *Nat. Photonics*, 5, 222 (2011).

[76] R. Demkowicz-Dobrzański, et al. *Nat. Commun.* 3, 1063 (2012).

[77] B. P. e. a. Abbott, *Phys. Rev. Lett.* 116, 061102 (2016).

[78] L. A. Correa, et al. *Phys. Rev. Lett.* 114, 220405 (2015).

[79] P. P. Hofer, et al. *Phys. Rev. Lett.* 119, 090603 (2017).

[80] A. Monras, F. Illuminati, *Phys. Rev. A* 83, 012315 (2011).

[81] M. A. Ballester, *Phys. Rev. A* 70, 032310 (2004).

[82] R. Gaiba, M. G. A. Paris, *Phys. Lett. A* 373, 934 (2009).

[83] F. Fröwis, et al. *New J. Phys.* 16, 083010 (2014).

[84] Y.-L. Zhang, et al. *Phys. Rev. A* 88, 052314 (2013).

[85] K. Matsumoto, *J. Phys. A: Math. Gen.* 35, 3111 (2002).

[86] C. Vaneph, et al. *Quan. Meas. and Quan. Metr.* 01, 12-20 (2013).

[87] M. Vidrighin, et al. *Nat. commu.* 05, 3532 (2014).

[88] P. Crowley, et al. *Phys. Rev. A* 89, 052108 (2014).

[89] S. Ragy, et al. *Phys. Rev. A* 94, 052108 (2016).

[90] L. Seveso, et al. *J. Phys. A: Math. Theo.* 53, 02LT01 (2019).

[91] P. Hauke, et al. *Nat. Phys.* 12, 778 (2016).

[92] C. Liu, et al. *Quan. Inf. Pro.* 16, 219 (2017).

[93] Naimy, Adnan, et al. "Optimal Multiparameter Quantum Estimation of Magnonic Couplings in a Magnomechanical Cavity." arXiv preprint arXiv:2511.12352 (2025).

[94] M. Asjad, et al. *Physical Review Research*, 5(1), 013185 (2023).

[95] P. Meystre, and M. Sargent, Springer Science & Business Media (2007).

[96] M. O. Scully M. S. Zubairy, *Quantum optics* (1999).

[97] R. Wolf, et al. *Opt. Express*, 25, 29927 (2017).

[98] J. Szabados, et al. *Phys. Rev. Lett.* 124, 203902 (2020).

[99] M. Wang, et al. *New J. Phys.* 22, 073030 (2020).

[100] D. Lachance-Quirion, et al. *Appl. Phys. Expr.* 12, 070101 (2019).

[101] Y. Tabuchi, et al. *Compt. Ren. Phys.* 17, 729-739 (2016).

[102] M. Tsang, C. M. Caves, *Phys. Rev. Lett.* 105, 123601 (2010).

[103] X. Xu, J. M. Taylor, *Phys. Rev. A* 90, 043848 (2014).

[104] B. Levitan, *New J. Phys.* 18, 093014 (2016).

[105] A. Motazedifard, et al. *Phys. Rev. A* 100, 023815 (2019).

[106] E. X. DeJesus, C. Kaufman, *Phys. Rev. A*, 35.12, 5288 (1987).

[107] D. Vitali, et al. *Phys. Rev. Lett.* 98.3, 030405 (2007).

[108] P. C. Parks, V. Hahn, Prentice-Hall, Inc. (1993).

[109] Q. Zheng, et al. *Eur. Phys. J. D*, 68.6, 170 (2014).

[110] H. Yuen, M. Lax, *IEEE Trans. Inf. Theory*, 19.6, 740-750 (2003).

[111] D. Safránek, *Journal of Physics A: Mathematical and Theoretical*, 52(3), 035304 (2018).

[112] L. Bakmou, M. Daoud, *J. Phys. A: Math. Theor.* 53.38, 385301 (2020).

[113] Y. Rozhin, et al. *Physical Review A* 95.6, 062307 (2017).

[114] M. G. Genoni, et al. *Phys. Rev. A: At. Mol. Opt. Phys.* 87.1, 012107 (2013).

[115] C. W. Helstrom, *J. of Stat. Phys.* 1.2, 231-252 (1969).

[116] Y. H. Yan, et al. *Chin. Phys. B* (2025).

[117] V. P. Belavkin, *Found. Phys.* 24.5, 685-714 (1994).

[118] A. S. Holevo, *Rep. Math. Phys.* 13.3, 379-399 (1978).

[119] V. Katariya, M. M. Wilde, *New J. Phys.* 23.7, 073040 (2021).

[120] R. Demkowicz-Dobrzański, et al. *Phys. A: Math. Theor.* 53.36, 363001 (2020).

[121] J. Suzuki, *Int. J. Quantum Inf.* 13.01, 1450044 (2015).

[122] J. Suzuki, et al. *Phys. A: Math. Theor.* 53.45, 453001 (2020).

[123] H. Yuan, C. H. F. Fung, *npj Quantum Inf.* 3.1, 14 (2017).

[124] A. Monras, F. Illuminati, *Phys. Rev. A*, 83 012315 (2011).

[125] A. Monras, F. Illuminati, *Phys. Rev. A* 81 062326 (2010).

[126] P. J. Crowley, et al. *Phys. Rev. A*, 89.2, 023845 (2014).

[127] A. Serafini, CRC press (2023).

[128] S. Ragy, et al. *Phys. Rev. A* 94.5, 1-11 (2016).

[129] J. Miyazaki, K. Matsumoto, *Quantum*, 6, 665 (2022).

[130] C. Vaneph, et al. *Quant. Measur. Quant. Metr.*, 1, 12-20 (2012).

[131] M. D. Vidrighin, et al. *Nat. Commun.* 5.1, 3532 (2014).

- [132] Y. Gao, and H. Lee, *Eur. Phys. J. D*, 68.11, 1-7 (2014).
- [133] C. L. Degen, F. Reinhard, and P. Cappellaro, *Rev. Mod. Phys.* 89.3, 035002 (2017).
- [134] J. Liu, et al. *Phys. A: Math. Theor.* 53.2, 023001 (2020).
- [135] M. G. Paris, *Int. J. Quantum Inf.* 7(supp01), 125-137 (2009).
- [136] C. Oh, et al. *npj Quantum Inf.* 5.1, 10 (2019).
- [137] J. X. Peng, et al. *Phys. Rev. A*, 109.2, 022601 (2024).
- [138] A. Monras, *arXiv preprint arXiv:1303.3682* (2013).
- [139] M. Aspelmeyer, et al. *Rev. Mod. Phys.* 86.4, 1391-1452 (2014).
- [140] X. B. Yan, *Opt. Express*, 27.17, 24393-24402 (2019).
- [141] Y. Shaked, *Nat. Commun.* 9.1, 609 (2018).
- [142] É. Rácz, *arXiv preprint arXiv:2310.18821* (2023).
- [143] G. Frascella, et al. *npj Quantum Inf.* 7.1, 72 (2021).
- [144] S. Feng, et al. *J. Opt. Soc. Am. B: Opt. Phys.* 33.7, 1365-1372 (2016).
- [145] C. Weedbrook, *Rev. Mod. Phys.* 84.2, 621-669 (2012).